Chapter 7
Design and Performance of High-Speed VCSELs

Yu-Chia Chang and Larry A. Coldren

Abstract Over the past several years, high-speed vertical-cavity surface-emitting lasers (VCSELs) have been the subject of intensive worldwide research due to their applications in optical interconnects and optical data networks. The performance of VCSELs, especially with respect to their high-speed characteristics, has made significant progress. In this chapter, we first present the basic theory for current-modulated VCSELs using rate equations and small-signal analysis. Factors that affect the modulation bandwidth, including the intrinsic laser responses and extrinsic parasitics, are identified. Once these limitations are known, we discuss various designs that have been implemented in VCSELs to specifically address them, followed by a review of the current high-speed VCSEL performance based on these designs at several different wavelengths, including 850 nm, 980 nm, 1.1 μm, and 1.3–1.6 μm. Finally, we consider new modulation schemes based on loss modulation in coupled-cavity VCSELs, which has the potential to reach even higher speeds.

7.1 Introduction

The rapid explosion of information has created ever increasing demands for data bandwidth. Optical fiber communication now dominates long-haul and metropolitan telecommunication networks, and it has made many in-roads into data-communication networks in campus and high-performance computing environments. However, traditional electrical signaling is still used for many tele- and data-communication links at the edge of these networks where data rates are still modest. But, even here

Y.-C. Chang (✉)· L. A. Coldren
Department of Electrical and Computer Engineering,
University of California, Santa Barbara, CA, USA
e-mail: yuchia@engineering.ucsb.edu

L. A. Coldren
e-mail: coldren@ece.ucsb.edu

Fig. 7.1 Timeline of the first reported 20, 25, 30, 35, and 40 Gb/s direct current modulation of VCSELs

optical techniques are beginning to look more attractive as the optical component cost becomes more competitive and the bandwidth demands increase. Also as space and power dissipation become important, some fundamental limitations come into play [1]. Optics is progressively replacing many electrical links, from networks to eventually even chip-to-chip and on-chip interconnects within computers. Low-cost, power-efficient, high-speed optical sources are one of the main keys to enable this transition.

Vertical-cavity surface-emitting lasers (VCSELs) are inherently suitable for optical data transmission for various reasons. Their small volume fundamentally implies that low power consumption and high-speed operation can be realized simultaneously. Due to surface emission, VCSELs can produce a more circular output beam with less divergence, can easily be fabricated in arrays, and can support on-wafer testing. All these lead to a significant reduction of the testing and packaging costs.

Over the past several years, worldwide research efforts to improve the performance of VCSELs for optical data links have reached fruition, especially with respect to their high-speed aspects. Figure 7.1 summarizes the timeline of the first reported data rates of 20, 25, 30, 35, and 40 Gb/s for directly modulated VCSELs. In 2001, 20-Gb/s operation was reported by Kuchta et al. using oxide-confined 850-nm VCSELs [2]. Not until 2006, 25-Gb/s operation was achieved by Suzuki et al. in NEC using 1.1-µm-wavelength VCSELs [3]. One year later, data rate was further pushed to 30 Gb/s by the same group using buried tunnel junction (BTJ) VCSELs [4]. Just after six months, a data rate of 35 Gb/s was reported by Chang et al. using oxide-confined 980-nm VCSELs [5]. Three months later, the 40-Gb/s milestone was finally hit by Anan et al., again by NEC, using BTJ VCSELs [6]. So, in the year 2007, the direct modulation speed of VCSELs was pushed from 25 to 40 Gb/s, a tremendous progress.

Of at least equal importance, many system-level optical links based on VCSELs have been demonstrated in this period. For example, an aggregate data rate of 500 Gb/s has been reported using 48 channels of 10.42-Gb/s data transmitted over a parallel 12-fiber ribbon with four wavelengths per fiber [7]. These links have demonstrated that power consumption is equally important to speed, so a significant emphasis on reducing overall power-consumption/data-rate ratio is also a goal for both optical interconnects and optical data links. The total link power consumption, including driver and receiver electronics, for 500 Gb/s is 3.3 W, corresponding to a power-consumption/data-rate ratio of 6.6 mW/(Gb/s). For waveguide-based

chip-to-chip optical links, an aggregate data rate of 160 Gb/s has been reported with
4×4 VCSEL and photodiode arrays, each operated at 10 Gb/s [8]. The total link
power consumption is 2.5 W, corresponding to 15.6 mW/(Gb/s). More results will be
presented in Chaps. 15 and 16 of this book.

Long-wavelength VCSELs (LW-VCSELs) have made significant progress as well.
Novel structures and new materials have been pursued to overcome the material
challenges faced by LW-VCSELs. Based on different technologies, several groups
and companies have demonstrated data transmission at 10 Gb/s over single-mode
fibers (SMF) [9–13]. At this writing such components are beginning to be sam-
pled commercially by some companies. Although intense efforts on 1300–1550 nm
VCSELs are expected to continue, it is unlikely that such devices will reach the
modulation bandwidths ultimately available in the shorter 850–1100 nm range due
to both material and cavity volume constraints that will be discussed in the next
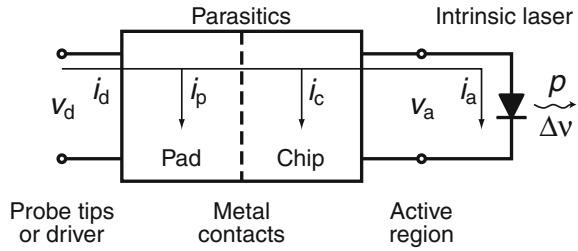section.

This chapter is organized as follows. Section 7.2 presents the theoretical back-
ground for current-modulated VCSELs. The device designs are covered in Sect. 7.3,
and Sect. 7.4 reviews some of the high-speed VCSEL results. Section 7.5 discusses
loss-modulated VCSELs, and Sect. 7.6 concludes this chapter.

7.2 Theoretical Background

Before jumping to the design of high-speed VCSELs, it is important to understand
how the bandwidth of VCSELs is determined. Once various factors that can limit the
bandwidth are known, the VCSEL structure can be specifically optimized to address
these restrictions. In this section, the necessarily theoretical background for directly
current modulating VCSELs is provided.

Just like other diode lasers, the bandwidth of VCSELs is determined by the intrin-
sic laser response as well as the extrinsic parasitic response. To facilitate our discus-
sion, the cascaded two-port model for representing a diode laser, shown in Fig. 7.2,
is used to separate the intrinsic laser and the parasitics [14]. The intrinsic laser is the
active region where it is desirable to concentrate the current and optical modes to
maximize the carrier and photon densities, which are coupled via stimulated recom-
bination. The parasitics, defined between the intrinsic laser and the driving circuit,
are split into the pad parasitics and chip parasitics at the metal contacts. The input
variables in the model are the drive voltage v_d and drive current i_d. The currents
entering the pad and chip parasitics are i_p and i_c, respectively. The voltage and cur-
rent seen by the intrinsic laser are v_a and i_a, respectively. The output variables are
the output power p and frequency shift $\Delta \nu$. For short-distance optical data links,
dispersion is usually not a concern and $\Delta \nu$ will not be considered.

Fig. 7.2 Cascaded two-port
model for VCSEL

7.2.1 Intrinsic Laser Response

Rate Equation Analysis

We start with the phenomenological rate equations, which describe the supply and
loss of the carriers and photons within the active region [15]:

$$\frac{dN}{dt} = \frac{\eta_i I}{qV} - \frac{N}{\tau} - v_g g N_p \tag{7.1a}$$

$$\frac{dN_p}{dt} = \Gamma v_g g N_p + \Gamma R'_{sp} - \frac{N_p}{\tau_p} \tag{7.1b}$$

where N is the carrier density, N_p is the photon density, η_i is the injection efficiency,
I is the terminal current, q is the electronic charge, V is the volume of the active region,
τ is the carrier lifetime, v_g is the group velocity, g is the gain, Γ is the confinement
factor, R'_{sp} is the spontaneous recombination rate into the mode of interest, and τ_p is
the photon lifetime.

The gain g can be well approximated by a four-parameter logarithmic formula
[15]

$$g(N, N_p) = \frac{g_0}{1 + \varepsilon N_p} \ln\left(\frac{N + N_s}{N_{tr} + N_s}\right) \tag{7.2}$$

where g_0 is the gain coefficient, ε is the gain compression factor, N_{tr} is the trans-
parency carrier density, and N_s is a shift to make g equal the unpumped absorption
at $N = 0$.

Once we have the rate equations ready, small-signal frequency analysis can be
applied. Assume there is a small sinusoidal modulating current with an amplitude of
I_1 superimposed on the steady-state bias current I_0, we have

$$I(t) = I_0 + I_1 e^{j\omega t} \tag{7.3a}$$

$$N(t) = N_0 + N_1 e^{j\omega t} \tag{7.3b}$$

$$N_p(t) = N_{p0} + N_{p1} e^{j\omega t} \tag{7.3c}$$

where N_0 and N_{p0} are the steady-state carrier and photon densities, N_1 and N_{p1} are the corresponding small-signal modulation amplitudes, and ω is the angular frequency. Substituting (7.3) into (7.1), neglecting the products of the small-signal terms, but retaining other first-order deviations, we obtain the modulation transfer function

$$H_{\mathrm{int}}(\omega) \equiv \frac{p(\omega)}{i_a} = A_i \frac{\omega_r^2}{(\omega_r^2 - \omega^2 + j\omega\gamma)} \qquad (7.4)$$

where A_i is the DC slope efficiency, $\omega_r = 2\pi f_r$ is the relaxation resonance frequency, and γ is the damping factor. This transfer function is in the form of a second-order low-pass filter with a damped resonance peak.

The relaxation resonance frequency is the natural oscillation frequency between the carriers and photons in the laser cavity and can be approximately expressed as

$$\omega_r = \left[\frac{v_g a N_{p0}}{\tau_p} \right]^{1/2} = \left[\frac{v_g a}{q V_p} \eta_i (I_0 - I_{th}) \right]^{1/2} \qquad (7.5)$$

where $a = \partial g / \partial N|_{\mathrm{th}}$ is the differential gain at threshold, V_p is the mode volume, and I_{th} is the threshold current. As clearly shown in (7.4), the relaxation resonance frequency basically determines how fast an intrinsic diode laser can be modulated when the damping is not severe. Therefore, it is important to increase the relaxation resonance frequency for higher bandwidth. Examining (7.5) tells that higher differential gain a, larger photon density N_{p0}, and smaller photon lifetime τ_p can improve the relaxation resonance frequency. (But, one must be careful not to think that adding internal loss is good, because it always reduces N_{p0} more than τ_p.)

The only parameter, to the first-order approximation, in (7.5) that depends on the operating conditions is the photon density, which can be increased with higher current. A figure of merit commonly used to evaluate how efficient an intrinsic laser can be modulated is the D-factor [16]

$$D \equiv \frac{f_r}{(I - I_{th})^{1/2}} = \frac{1}{2\pi} \left[\frac{v_g a}{q V_p} \eta_i \right]^{1/2} .$$

To evaluate the device's overall high-speed performance, the related factor, modulation current efficiency factor (MCEF), is more commonly used [17]

$$\mathrm{MCEF} \equiv \frac{f_{3\mathrm{dB}}}{(I - I_{th})^{1/2}}$$

where $f_{3\mathrm{dB}}$ is the 3-dB frequency, which is approximately equal to $1.55 f_r$ when the parasitics and damping are relatively small.

The damping represents the rate of energy loss in the laser cavity, which effectively reduces the strength of the resonance peak. The damping factor γ is given as

$$\gamma = v_g a N_{p0} \left[1 + \frac{\Gamma a_p}{a} \right] + \frac{1}{\tau_{\Delta N}} + \frac{\Gamma R'_{sp}}{N_{p0}} \qquad (7.6)$$

where $\tau_{\Delta N}$ is the differential carrier lifetime, and

$$a_{\mathrm{p}} = -\left.\frac{\partial g}{\partial N_{\mathrm{p}}}\right|_{N_{\mathrm{p}0}} = \frac{\varepsilon g}{1 + \varepsilon N_{\mathrm{p}0}}. \tag{7.7}$$

At normal high-speed operating conditions, spontaneous-emission-related damping can be neglected, and γ increases with $N_{\mathrm{p}0}$, which is proportional to f_{r}^2. The proportionality is the K-factor given as

$$K = 4\pi^2 \tau_{\mathrm{p}} \left[1 + \frac{\Gamma a_{\mathrm{p}}}{a} \right]. \tag{7.8}$$

Practically, K-factor is empirically determined by fitting γ versus f_{r}^2. As the photon density keeps increasing to a point, the modulation response becomes overdamped and the bandwidth decreases. The maximum theoretically damping-limited f_{3dB} is given as

$$f_{\mathrm{3dB}}|_{\mathrm{max}} = \sqrt{2}\frac{2\pi}{K} \qquad (\gamma/\omega_{\mathrm{r}} = \sqrt{2}). \tag{7.9}$$

Since K-factor increases with gain compression factor ε through a_{p}, reducing gain nonlinearity is also important to achieve high bandwidth.

Beyond the Rate Equations

The proceeding rate equation analysis is appealing due to its simplicity but still providing intuitive insights. However, many effects were not included, and we summarize some of them here.

First discovered in 1991, carrier transport in the separate-confinement heterostructure (SCH) region actually plays an important role in the dynamics of quantum-well (QW) lasers [18]. To reduce the carrier transport effects, it is necessary to minimize the time for carriers to reach and fall into QWs and maximize the time for carriers to escape back from QWs to SCH region. This can be treated with a modified set of rate equations that incorporates a second carrier reservoir [15], but we shall not go into that complexity here.

We also have implicitly assumed that the carrier and photon densities are uniform across the active region in (7.1a) and (7.1b). In reality, the photon density varies spatially as the square of the optical mode field due to the waveguiding of the cavity, which causes the stimulated emission rate to vary accordingly. This spatial non-uniformity of the stimulated emission rate results in an overdamping of the relaxation resonance frequency, which reduces the bandwidth [19]. In addition, carriers are depleted faster where the optical intensity is higher, a phenomenon referred to as *spatial hole burning*, and the carrier gradient drives diffusion [20]. It has been shown that the lateral carrier diffusion does not significantly reduce the bandwidth but increases the damping [21].

In (7.2), the nonlinearity of gain was included through the gain compression factor ε. This saturation of gain at high photon density is attributed to the *spectral*

hole burning and carrier heating effects [22]. It is important to minimize the gain nonlinearity so that damping can be reduced.

Many parameters in the rate equations are actually temperature dependent. Excessively high junction temperature degrades the differential gain, reduces the injection efficiency, increases the threshold current, affects the transverse modes, and redshifts the cavity mode and gain peak. All these lead to a reduction of the bandwidth. Therefore, thermal management is a main issue for high-speed VCSELs.

Many of the limitations on modulation bandwidth are more acute in the longer wavelength VCSELs, especially the thermal effects due to the relative importance of Auger recombination. Thermal management is even more important, but quaternary materials tend to have very poor thermal conductivities, so additional 'engineering fixes' are required. Gain materials at longer wavelengths also usually have lower inherent differential gain, and the cavity volume tends to be larger because of lower inherent index contrast for lattice-matched alloys, which either directly results in a longer mirror, or requires an intracavity contact.
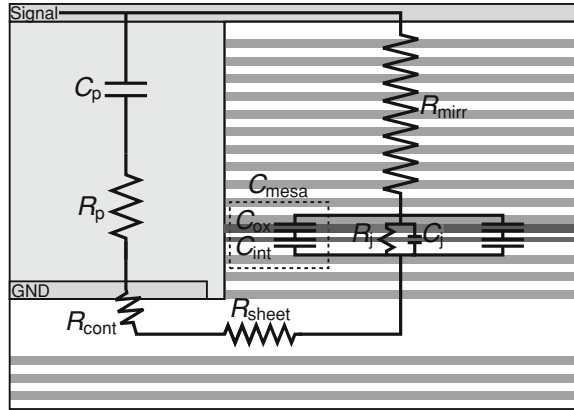
7.2.2 Extrinsic Parasitic Response

When dealing with high-frequency devices, parasitics are always a concern. Parasitics divert the modulated current i_d from entering the intrinsic laser due to i_p and i_c. In most cases, it is desirable to minimize the parasitics so that the intrinsic bandwidth can be achieved.

The parasitics vary depending on the device structure. Here a typical oxide-confined VCSEL, whose cross-sectional schematic and parasitic elements are shown in Fig. 7.3, is used as an example. The pad capacitance C_p represents the capacitance between the signal and ground from the probe tips/driver to the metal contacts. The value of C_p varies from tens to hundreds of femto-farads, depending on the pad layout and the materials between the pads. The pad resistance R_p accounts for the pad loss. Since it is usually relatively small, in the ohm range, compared with the impedance of C_p at the frequency of interest, it is sometimes omitted in the small-signal model.
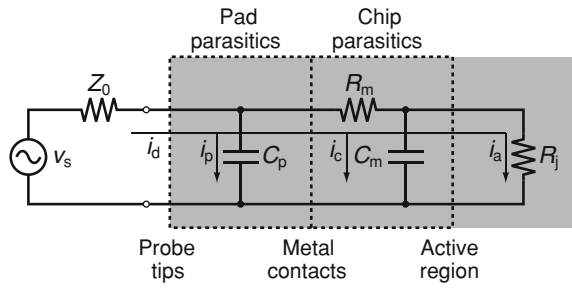
The mirror resistance R_{mirr} includes the resistances from both DBRs. It includes the net differential impedances of the mirror heterobarriers at the bias point. R_{sheet} represents the sheet resistance in the n-contact layer, and R_{cont} is the contact resistance for both contacts. All these resistances, usually dominated by R_{mirr}, can be grouped together into $R_m = R_{mirr} + R_{sheet} + R_{cont}$ in the small-signal model. The mesa capacitance C_{mesa} is the oxide capacitance in series with the capacitance associated with the intrinsic region below the aperture. C_{mesa} depends on the diameters of the mesa and aperture and the thicknesses of the oxide and intrinsic semiconductor layer.

The capacitance C_j represents the diode junction capacitance in the apertured area where current flows. Under normal forward bias condition, C_j is usually dominated by the diffusion capacitance, which models the modulation of the minority carriers stored in the intrinsic SCH [23]. It has been shown that the diffusion capacitance not only depends on the carrier lifetime but also depends on the design of the SCH [24].

Fig. 7.3 Cross-sectional schematic of an oxide-confined VCSEL superimposed with its parasitics

Fig. 7.4 Small-signal model with the driving source. The grayed area represents the VCSEL

For simplicity, C_{mesa} and C_j are grouped together into $C_m = C_{mesa} + C_j$. Lastly, the intrinsic laser is represented by the junction resistance R_j.

Figure 7.4 plots the small-signal model of VCSEL and the RF driving source. The VCSEL is represented by four elements, including C_p, R_m, C_m, and R_j. The RF driving source consists of a voltage source v_s and a characteristic impedance of Z_0. Here we have assumed that the device is driven by 50-Ω-terminated instruments, and Z_0 is included to account for the RF power reflection due to impedance mismatch.

The effects of the parasitics can be described by a transfer function, $H_{ext}(\omega)$ [25]:

$$H_{ext}(\omega) \equiv \frac{\text{current flowing into the intrinsic diode}}{\text{voltage from the voltage source}} = \frac{i_a(\omega)}{v_s}.$$

The frequency at which $|H_{ext}(\omega)|^2/|H_{ext}(0)|^2 = 1/2$ is defined as the parasitic 3-dB frequency ω_{rc}. This transfer function can be approximated by a single-pole low-pass filter function:

$$H_{ext}(\omega) = \frac{A_e}{1 + j\omega/\omega_0} \tag{7.10}$$

where A_e is a proportional constant and ω_0 is the parasitic roll-off frequency, which may be different from ω_{rc}.

The overall electrical modulation frequency response $H(\omega)$ is given as:

$$H(\omega) \equiv \left|\frac{p(\omega)}{v_s}\right|^2 = \left|\frac{i_a(\omega)}{v_s} \cdot \frac{p(\omega)}{i_a(\omega)}\right|^2 = |H_{ext}(\omega) \cdot H_{int}(\omega)|^2$$
$$\propto \left(\frac{1}{1 + (\omega/\omega_0)^2} \frac{\omega_r^4}{\left(\omega_r^2 - \omega^2\right)^2 + \gamma^2 \omega^2}\right). \tag{7.11}$$

This gives the commonly used three-pole equation, which is squared when considering electrical-to-electrical links, for fitting the frequency response to extract ω_r, γ, and ω_0.

7.3 Design of High-Speed VCSELs

In Sect. 7.2, we have discussed various factors that can affect the bandwidth of VCSELs based on small-signal analysis. Now we will review different designs to specifically address these limitations for better high-speed performance.

7.3.1 Active Region

The choice of active region is mainly determined by the wavelength and the substrate. However, some designs are better than the others in terms of high-speed performance. Most of them are related to the improvement in differential gain. Differential gain depends on the sensitivity of the quasi-Fermi levels (and thus gain) to small changes in carrier density [15]. To have higher differential gain, the density of states (DOS) needs to be more peaked near the band edges, and the quasi-Fermi levels, where the slopes of the Fermi functions are at their maximum, need to be aligned to the band edges.

In order to improve differential gain, a number of refinements to the active region have been explored. Originally, quantum dots (QDs) were proposed as a superior gain region because of their inherent delta-function-like DOS, which should have a huge differential gain [26], but all experimental QDs have a very broad DOS due to variable dot size and the associated inhomogenous broadening. Adding strain in the QWs reduces the anisotropy between the DOS of electron and hole as well as pushes the hole quasi-Fermi level towards the valence band edge, which improves differential gain [15, 27]. In addition, strain advantageously reduces the transparency carrier density [15]. However, gain nonlinearity and damping increase with strain due to the increased valance-band curvature [22]. P-doping the active region increases the carrier-carrier scattering rate and thus decreases the intraband relaxation times, which reduces the gain nonlinearity induced by spectral hole burning [27]. P-doping also moves the quasi-Fermi levels down to a more symmetrical position and can increase

the differential gain [15]. However, the experimentally observed improvement in differential gain due to *p*-doping is more pronounced in unstrained systems than in strained systems [28]. In short, strained QWs perform better than unstrained QWs due to higher differential gain, and *p*-doped strained QWs perform better than undoped strained QWs due to reduced gain nonlinearity.
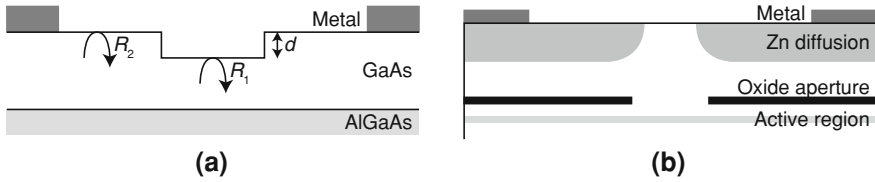
Within the strain limit, increasing the number of QWs is generally preferable for high-speed operation due to the differential gain enhancement [29]. However, the gain enhancement factor from the standing-wave effect, unique for VCSELs, decreases with increased number of QWs and must be considered [15]. Deeper wells are also favorable for high-speed and high-temperature operation because carriers have less chance to escape from the QWs, which reduces the carrier transport effects and carrier leakage.

7.3.2 Lateral Mode Confinement and Single Modeness

Since the relaxation resonance frequency increases with the square root of the photon density, it is desirable to increase the photon density for high-speed operation. This can be done by (1) increasing the current above threshold that contributes to the number of photon, i.e., $\eta_i(I-I_{th})$, (2) reducing the mode volume, and (3) maintaining single-mode operation to insure that the photon density must increase as the current increases. For given device dimensions and bias current, single-mode devices have higher photon density because photons do not spread among the mutually orthogonal modes. Maintaining single-mode operation is also necessary for some applications which use SMF or require better beam quality. However, some past applications have desired multimode VCSELs to match multimode fibers or waveguides. Unfortunately, these are not well suited for high data rate applications. Here we will mention some approaches to achieve single-mode operation, and more details can be found in Chap. 5 of this book.

For gain-guided VCSELs without any deliberate index guiding, the lateral mode confinement is mainly provided through thermal lensing effects, which can be unstable under dynamic operation due to time-dependent temperature variation [30]. Although gain-guided VCSELs have demonstrated 14.5 GHz modulation bandwidth [31], index guiding is more common nowadays for high-speed VCSELs, both to insure single mode operation, as well as reduce the mode volume.

The most common approach to implement lateral index guiding, at least for GaAs-based VCSELs, is to use a dielectric aperture. The discovery of wet thermal oxidation of high aluminum content semiconductors provides an easy way to form thermally stable aluminum oxide inside a VCSEL cavity. Oxide-confined VCSELs have shown superior performance in many aspects due to reduced internal losses, and simultaneously providing good electrical and optical confinement. Various aperture designs have been incorporated in high-speed VCSELs, including standard quarter-wavelength-thick blunt aperture [32], double apertures [33, 34], thin aperture (∼30 nm) [35], and tapered oxide aperture [36, 37].

Fig. 7.5 Two approaches to achieve single-mode VCSELs. **a** Illustration of the inverted surface relief structure on the top surface of a VCSEL. Reflectivity R_2 is lower due to an extra thickness of d, and the center is etched down to restore the high reflectivity R_1 for the fundamental mode. **b** Illustration of Zn diffusion from the top surface to create a higher-order mode absorber

There are several advantages of using a tapered oxide aperture. First, it can achieve lower optical scattering losses if designed properly [38, 39]. This is because a tapered oxide aperture, if placed at the standing-wave node, can produce a nearly ideal parabolic lens that eliminates the optical scattering loss. Second, the nonlinear damping effects can be reduced for higher bandwidth by confining the current smaller than the optical mode [19, 40]. Third, the parasitic capacitance from the oxide can be lower due to the increased oxide thickness at high radii where the area is large. Fourth, the eigenmodes are Hermite–Gaussian modes, which diffract less and have no sidelobes, so that external coupling and focusing can be done more ideally. On the other hand, a tapered oxide aperture also reduces the losses that differentiate the fundamental and higher-order modes, and the devices tend to be multi-mode unless some mode-dependent loss is added. Fortunately, the higher-order modes have significantly larger diameters, so this can also be done more easily than in other cases.

Approaches have been proposed to achieve single-mode operation for larger-diameter devices, which can also be implemented for tapered-oxide-apertured devices. Many of them involve creating some mode-dependent losses, usually in the perimeter of the top mirror, to favor the more centered fundamental mode. For example, a surface relief structure, as illustrated in Fig. 7.5a, increases the mirror loss [41], or Zn diffusion, shown in Fig. 7.5b, increases the internal loss for the higher-order modes [42]. High-speed, single-mode VCSELs have been demonstrated with these two approaches [13, 43].

Aperturing using an etched tunnel junction and then performing a regrowth over it to form a BTJ, which is common for InP-based LW-VCSELs, can also provide mode confinement as well as current confinement. This is due to the larger optical cavity length, where the unetched tunnel junction material remains in the center of the cavity. Single-mode operation can be achieved with BTJ for diameters up to 7 and 9 μm at 1.3- and 1.55-μm wavelengths, respectively [44].

7.3.3 Chip Parasitics

Parasitics are one of the main limiting factors for high-speed VCSELs. As can be seen in Table 7.1, most devices have relatively close f_{3dB} and f_{rc}, indicating they are

Table 7.1 Parasitic elements for different high-speed VCSELs from the literature

Authors	Lear	AL-Omari	Chang	Lin	Suzaki	Yashik
Reference	[45]	[32]	[46]	[47]	[3]	[4]
λ (μm)	0.85	0.85	0.98	0.98	1.1	1.1
Size (μm^2)	4×4	$3.5^2\pi$	$1.5^2\pi$	$3^2\pi$	$3.5^2\pi$	$2.5^2\pi$
I_0 (mA)	N/A	4.5	4.5	6.0	7.0	4.0
C_p (fF)	41.7	62	29	22	56	33
R_p (Ω)	15.9	17	0	0	0	0
R_m (Ω)	28.3	45	103	34.1	63.3	38
C_m (fF)	44.3	151	87.9	152	133	130
R_j (Ω)	288.7	64.4	146.5	92.0	71.6	134
f_{rc} (GHz)	36.4	21.8	22.8	22.5	23.6	21.0
f_{3dB} (GHz)	21.5	17	>20	17	20	24[a]

[a] Obtained from 5-μm-diameter devices

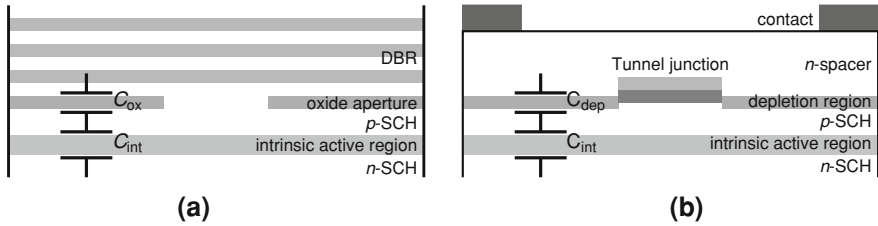partially parasitic-limited. In the following, we will discuss approaches to reduce the parasitics.

Chip Parasitic Resistance

Due to the alternating layers in the DBR mirrors, VCSELs inherently have much higher series resistance, ranging from tens to hundreds of ohms, compared with edge emitters. This excess resistance can limit the modulation bandwidth due to *RC* limitations and heating. Various bandgap-engineering schemes at the DBR interfaces, mostly for the *p*-mirror, have been proposed to simultaneously achieve low resistance and loss [48, 49]. Since *n*-type materials are less lossy and resistive, *p*-down configuration has also been pursued for top-emitting VCSELs [32, 50].

To eliminate the resistances and losses from the doped semiconductor DBR mirrors, one or both intracavity contacts with (partially) undoped semiconductor mirror/abrupt interfaces, mostly for oxide-confined VCSELs [35, 36], or dielectric DBR mirror, mostly for BTJ VCSELs with a regrown *n*-spacer for lower loss [6, 51], have been used. For dielectric DBR, several periods usually provide sufficient reflectivity due to large index contrast, which helps to compress the optical modes in the longitudinal direction. However, the uniformity of current injection, lateral sheet resistance, and optical loss from the highly-doped contact layers near the active region can be issues for intracavity contacts and must be considered in the device design [39].

Chip Parasitic Capacitance

Another source of the parasitics is the shunt mesa capacitance surrounding the active region. Figure 7.6 illustrates the sources of the mesa capacitance for oxide-confined and BTJ VCSELs. For oxide-confined VCSELs, the shunt mesa capacitance is the oxide capacitance C_{ox} in series with the capacitance from the intrinsic active region below the oxide aperture C_{int}. For BTJ VCSELs, the oxide capacitance is replaced by the depletion capacitance C_{dep} from the reverse-biased *p*–*n* junction.

Fig. 7.6 Schematics illustrating parasitic mesa capacitance for **a** oxide-confined VCSEL and **b** BTJ VCSEL

Since all these layers are relatively thin, the mesa capacitance can be quite large. Combined with high series resistance, parasitics can greatly reduce the achievable bandwidth. To reduce the mesa capacitance, it is necessary to create additional (thick) nonconducting layers inside the mesa above or below these high-capacitance current blocking junctions, and this is commonly done using implantation [6, 37, 50]. For oxide-confined VCSELs with semiconductor mirrors, the nonconducting layers can also be formed by oxidizing additional one (double aperture) [34] or several higher aluminum layers (deep oxidation layers) [36]. This can be performed simultaneously with the oxide aperture to eliminate one fabrication step. Since the dielectric constant for the aluminum oxide is much smaller than that of the semiconductor, the total thickness of the nonconducting layers can be smaller. This reduces the funneled distance, usually at the lowest-doped layers, that current has to conduct, which is beneficial for resistance.

For edge emitters, which typically work at relatively high currents, the junction resistance is practically negligible. Therefore, the diffusion capacitance, which is in parallel with the junction resistance, can be neglected. However, this is not the case for VCSELs due to their small currents. The junction resistance and diffusion capacitance have to be considered. A graded SCH layer can potentially reduce the diffusion capacitance [23] and has been employed in high-speed VCSELs [33].

7.3.4 Pad Parasitics

Since the pad parasitics are in parallel with the current path of the intrinsic laser, it is important for these to have a high impedance, i.e., smaller pad capacitance and higher pad shunt resistance, to prevent current flowing through them.

Reasonable size pads are necessary to drive VCSELs, especially for bonding. However, the associated pad parasitics can greatly reduce the modulation bandwidth if precautions are not taken. For example, the pad capacitance for a $100 \times 100\,\mu\text{m}^2$ pad on a 200-nm-thick nitride is $\sim 3.3\,\text{pF}$, which is very large (see Table 7.1). To overcome this limitation, some thick low-dielectric-constant resin can be used underneath the signal pad. The two most common choices are polyimide [32, 50] and

benzocyclobutene (BCB) [34, 36], although silicon dioxide has also been used [37]. Just as a comparison, the same 100×100 µm^2 pad on a 5-µm-thick BCB gives a pad capacitance of ∼47 fF, a 70 times reduction.

VCSELs grown on semi-insulating substrates can also have lower pad parasitics through co-planar transmission lines with lower microwave loss due to the removal of the resistive substrate. Similarly, removing the part of the contact layer that is underneath the signal pad also reduces the pad capacitance by enabling a higher impedance co-planar interconnecting line [5].
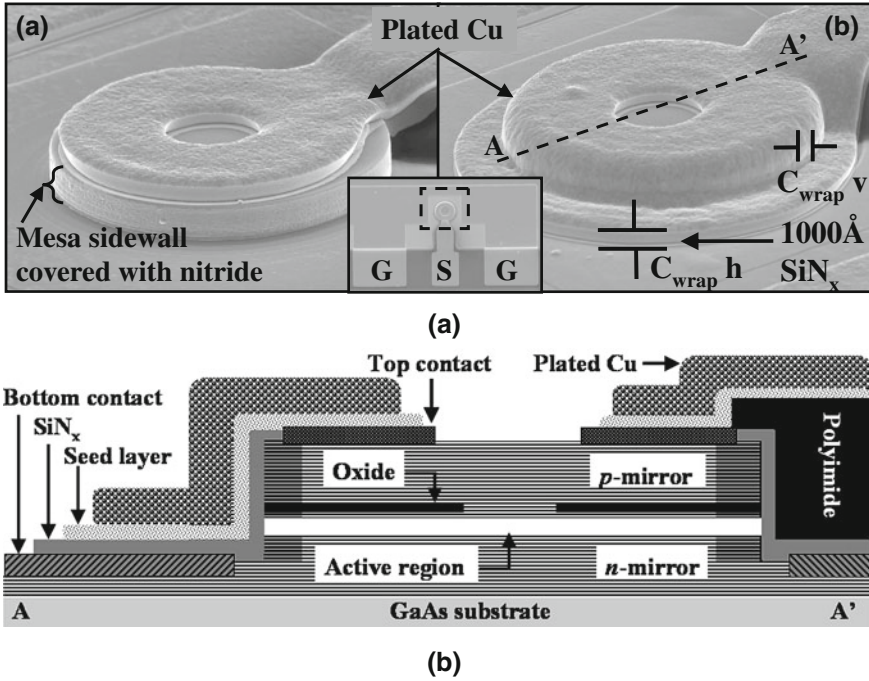
7.3.5 Thermal Management

Thermal management is always an important issue for high-speed devices. For VCSELs, most of the heat generated in the diode junction and DBRs is dissipated through the substrate. To more efficiently remove the heat, we can either integrate the devices on a substrate with higher thermal conductivity [52], e.g., copper which has ∼9 times of the thermal conductivity of GaAs, or provide additional heat sinking from the top surface and sidewalls using gold [53] or copper plating [54]. Compared with gold, copper is inexpensive and has high thermal conductivity, which makes it really attractive.

Figure 7.7 shows SEMs and schematic cross-section of copper-plated VCSELs [54]. The 4-µm-overlapped devices show considerably better thermal properties compared with the non-overlapped devices. This is because heat first flows laterally to the sidewalls and can eventually dissipate in the substrate through the copper, bypassing the more thermally-resistive bottom DBR. However, this relies on good thermal contact between the overlapped copper and substrate and would result a high parasitic capacitance if a thin dielectric is used. This trade-off can be addressed using flip-chip bonding so that heat can be dissipated through the bonded interface instead of the substrate, which relieves the restriction of the thickness of the dielectric layer [45].

In addition to improve heat dissipation, reducing the amount of heat generated is another way to prevent thermal degradation. Ideally, the relaxation resonance frequency should increase as the square root of the current density $J_0 = I_0$/Area. For a given current density, the temperature rise should be *lower* for smaller devices because power dissipation is roughly proportional to the area and thermal impedance is inversely proportional to the diameter [15]. However, smaller devices typically suffer from higher losses. If the size-dependent losses can be minimized, scaling the devices down should yield better performance. Size-dependent losses have been reduced by incorporating tapered apertures and this has allowed much smaller devices to be created with high bandwidths [55]. Perhaps more importantly, these smaller devices have lower currents for a given bandwidth, and a data-rate/power dissipation of 35 Gbps/10 mW has been reported [5].

Once the operating temperature is determined by the ambient temperature, heat generation and dissipation, the devices have to be optimized at that temperature.
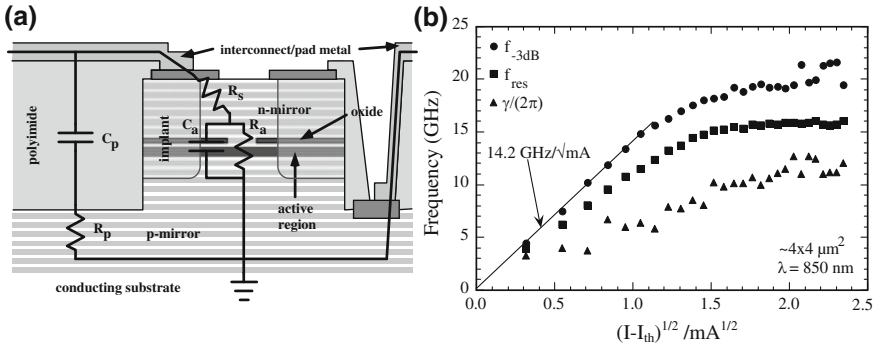
Fig. 7.7 **a** SEMs of copper-plated VCSELs. *Left*: heat sink from the top surface. *Right*: heat sink from both the top surface and sidewalls with 4-µm overlap with the substrate. **b** Cross-sectional schematic of the device [54] (© 2006 IEEE)

As the temperature increases, both the cavity mode and gain peak red-shift, but at different rates. Take 980-nm VCSELs with InGaAs QWs as an example, cavity-mode and gain peak shift at approximate 0.07 and 0.3 nm/°C, respectively [39]. By deliberately detuning the cavity-gain offset at room temperature, better high-temperature performance has been realized [56].

7.4 Performance of High-Speed VCSELs

This section reviews some of the high-speed VCSEL results at several different wavelengths. High-speed VCSELs operated at the datacom wavelengths, ranging from 0.83 to 1.1 µm, are exclusively GaAs-based and mainly for optical interconnects and short-distance optical links. Typical wavelengths include 850 nm, 980 nm, and 1.1 µm. LW-VCSELs operated at 1.3 and 1.55 µm are attractive as alternative light sources for optical links transmitting longer distances over SMF due to the low loss and dispersion of fibers at these wavelengths; both GaAs- and InP-based devices exist at the longer wavelengths.

Fig. 7.8 **a** Device structure and **b** f_{3dB}, f_r, and $\gamma/(2\pi)$ vs. $(I - I_{th})^{1/2}$ for the 850-nm VCSELs with a bandwidth of 21.5 GHz [45] (© 1997 OSA)

7.4.1 850-nm VCSELs

VCSELs operating at 850-nm wavelength are probably the most mature VCSEL technology to date, because 850 nm has several fiber-based standards for short-haul datacom. Products using 850-nm VCSELs for 10 Gigabit Ethernet have been commercially available on the market for some time.

There are several active region choices for 850-nm emission including GaAs/AlGaAs [37], InGaAs/AlGaAs [34], InAlGaAs/AlGaAs [57], and InGaAsP/InGaP [58]. We will focus on the GaAs/AlGaAs and InGaAs/AlGaAs designs, which are more common nowadays.

GaAs/AlGaAs 850-nm VCSELs

The unstrained GaAs/AlGaAs multiple quantum wells (MQW) is the most common active region choice for 850-nm VCSELs, and many high-speed records were achieved with it. For example, the first VCSEL to demonstrate a bandwidth in excess of 20 GHz was achieved with this active region in 1997, and this is still the highest reported bandwidth for 850-nm VCSELs [50]. Figure 7.8 shows a cross-sectional schematic and f_{3dB}, f_r, and $\gamma/(2\pi)$ vs. $(I - I_{th})^{1/2}$ for the $4 \times 4 \ \mu m^2$ devices that achieved a 21.5-GHz bandwidth.

One of the reasons that these devices achieved a high bandwidth was their low-parasitic structure (see the first column of Table 7.1). The pad capacitance is only 42 fF using 5-μm-thick polyimide underneath the pad. The pad resistance is due to the dielectric loss of the polyimide. The series resistance is reduced to 28.3 Ω using n-up configuration. Despite the junction resistance is 289 Ω, high-dose proton implantation brings C_m down to 44.3 fF so that current still flows through the intrinsic laser. Since $f_{rc} = 36.4$ GHz, the bandwidth is not parasitic-limited. Because the relaxation resonance frequency and 3-dB frequency both saturate at about the same current, the bandwidth is limited by the intrinsic laser response. The damping-limited

bandwidth, extracted from *K*-factor, is 58 GHz. Therefore, the devices are limited by thermal effects.

The highest data rate reported for 850-nm VCSELs with GaAs QWs is 30 Gb/s at a bias current of 8 mA using 6-μm-diameter devices [37]. The maximum bandwidth is 19 GHz at that bias.

InGaAs/AlGaAs 850-nm VCSELs

One of the issues with unstrained GaAs/AlGaAs QWs is that it has lower differential gain compared with strained QWs. It has been shown that adding some indium, typically 10% or less, in the wells can double the achievable gain and differential gain [59]. In addition, the presence of indium has been shown to suppress the propagation of dark-line defects, which prevents sudden failure of the devices [60]. Data rates of 32 Gb/s [61] and 39 Gb/s [62] have been demonstrated using 850-nm VCSELs with InGaAs QWs.

The 9-μm devices which achieved 32-Gb/s operation at 25°C have a threshold current of 0.6 mA, fairly low for this size, and a slope efficiency of 0.8 W/A, which corresponds to a differential quantum efficiency (DQE) of ~55%. The parasitics are reduced using BCB, an undoped substrate, double oxide apertures, and bandgap-engineered DBRs. The series resistance is approximately 90 Ω. They also reported 25-Gb/s operation up to 85°C.
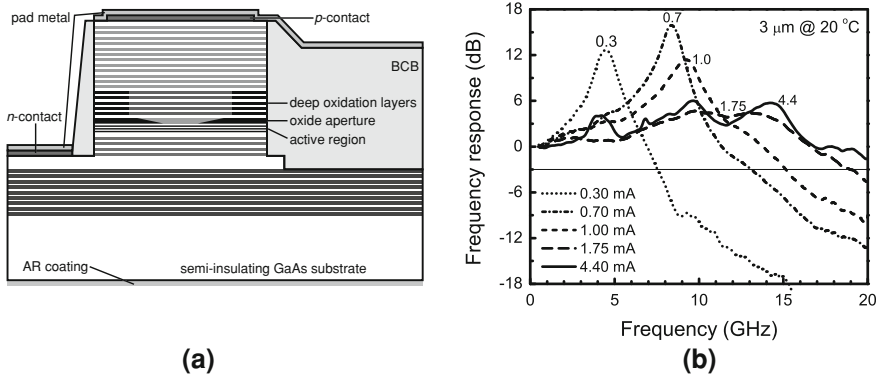
The devices that achieved a 39-Gb/s data rate have a diameter of ~6 μm, confined by an oxide aperture. BCB is used for reducing the pad parasitics, and a relatively large lower mesa for the bottom DBR is used for better heat dissipation, lower resistance, and easier manufacturing. The bias current for large-signal modulation is 9 mA, corresponding to a fairly low current density of ~10 kA/cm^2. Eye diagram at 40 Gb/s is also shown. The signal-to-noise ratio reduces from above 6.3 to 3.6, preventing error-free operation at 40 Gb/s.

7.4.2 980-nm VCSELs

Another common wavelength for high-speed VCSELs is 980 nm, which typically employs strained InGaAs/GaAs QWs. This aluminum-free active region offers high differential gain, low transparent carrier density, and superior reliability. Due to the transparency of GaAs substrates at 980 nm, bottom-emitting structure is commonly used.

InGaAs/GaAs 980-nm VCSELs

The highest MCEF for any QW-based VCSELs to date is 16.8 GHz/mA$^{1/2}$ using InGaAs/GaAs VCSELs at 970 nm [33]. One of the keys to achieve such high MCEF is the small mode volume. The dimensions of the devices are 3×3 μm^2, confined with double oxide apertures. Pad capacitance is estimated to be 40 fF for a 75×120 μm^2 bond pad. The threshold current is 0.37 mA and the DQE is 45%. The bandwidth

Fig. 7.9 a Structure and **b** frequency responses for 3-µm-diameter devices achieving 35-Gb/s operation
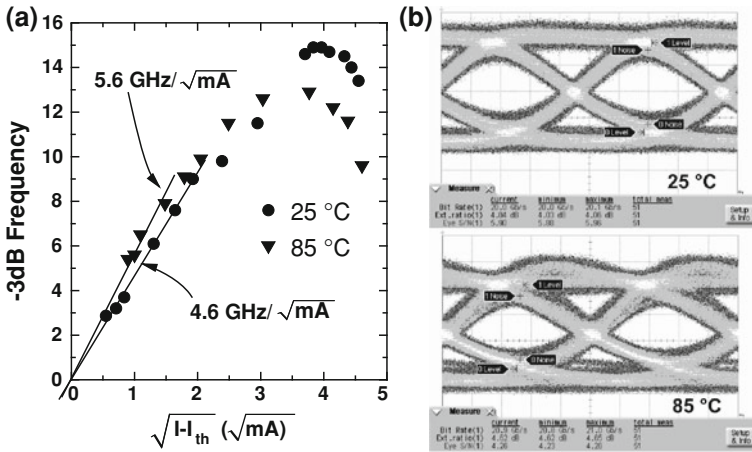
reaches 11.2 GHz at a bias current of only 1 mA, and the maximum bandwidth is 16.3 GHz at 4.5 mA.

The highest data rate reported for 980-nm VCSELs is 35 Gb/s using the structure shown in Fig. 7.9a [5]. Instead of the conventional quarter-wavelength-thick blunt oxide aperture, a half-wavelength-thick tapered oxide aperture is used. The taper length is carefully chosen to provide sufficient mode confinement while still maintaining low optical scattering losses [55]. This enables the smaller 3-µm devices, which typically suffer from high optical losses, to be used. The low pad capacitance of 29 fF is realized by using BCB, selectively etching off the *n*-GaAs contact layer underneath the signal pad, and shrinking the pad dimensions. Deep oxidation layers as well as the thick oxide aperture effectively reduce C_m down to ~88 fF. The devices have a threshold current of only 0.14 mA and a slope efficiency of 0.67 W/A (DQE = 0.54). The series resistance is approximately 250 Ω.

Figure 7.9b plots the frequency responses of the devices at 20°C. Due to the small size, a bandwidth of 15 GHz is achieved at a bias current of only 1 mA, corresponding to a power dissipation of 1.3 mW. The temperature rise is estimated to be 4.3°C. It is evident that small devices are more efficient and can achieve the bandwidth with lower currents and temperature rise, even with a somewhat higher series resistance than desired in this case. A bandwidth exceeding 20 GHz is also demonstrated for currents larger than 2 mA. The bandwidth is limited by multimoding above 2 mA; simulations illustrate that the maximum bandwidth would be ~25 GHz if single-mode operation were maintained. The MCEF at low biases is 16.7 GHz/mA$^{1/2}$. 35-Gb/s operation was achieved with a bias current of only 4.4 mA. This corresponds to a very high data-rate/power-dissipation ratio of 3.5 (Gb/s)/mW.

InAs QD 980-nm VCSELs

Another active region choice for 980-nm VCSELs is submonolayer deposited quantum dots, which provides higher differential gain and better temperature

Fig. 7.10 a f_{3dB} vs. $(I - I_{th})^{1/2}$ and **b** 20-Gb/s eye diagrams for 6-μm QD VCSELs at 25°C and 85°C [63] (© 2006 SPIE)

insensitivity [63]. Their 1-μm single-mode devices show the highest MCEF of 19 GHz/mA$^{1/2}$ for any VCSELs to date. For their 6-μm multimode devices, the threshold currents at 25°C and 85°C are 0.29 and 0.16 mA, respectively, due to better cavity–gain alignment at elevated temperatures.

Figure 7.10 shows f_{3dB} vs. $(I - I_{th})^{1/2}$ and eye diagrams for 6-μm devices at 25°C and 85°C. The MCEF drops from 5.6 to 4.6 GHz/mA$^{1/2}$ for the temperature increased from 25°C to 85°C. The maximum bandwidth at 25°C and 85°C are 15 and 13 GHz, respectively. These bandwidths still can support 20-Gb/s operation as shown in the eye diagrams. The eye is slightly degraded at 85°C. Recently, they demonstrated 20-Gb/s operation up to 120°C using 2-μm single-mode devices [64].

7.4.3 1.1-μm VCSELs

High-speed VCSELs operating in the 1.1-μm-wavelength range have resulted from engineering the MQW InGaAs/GaAs active region to have the maximum allowable strain as well as p-type modulation doping [65]. The active region consists of three thin highly-strained In$_{0.3}$Ga$_{0.7}$As/GaAs (5/10 nm) QWs. The GaAs barriers are modulation doped p-type at 2×10^{18} cm^{-3} to reduce gain nonlinearity. Two types of device structures have been reported: oxide-confined VCSELs and BTJ VCSELs.

Figure 7.11a shows their oxide-confined VCSEL structure. The 6.9-μm-diameter devices have a threshold current of 0.4 mA and a series resistance of 135 Ω. Because the mesa is relatively large at 33 μm in diameter, proton implantation is used to reduce the mesa capacitance. The pad capacitance is lowered using polyimide. The
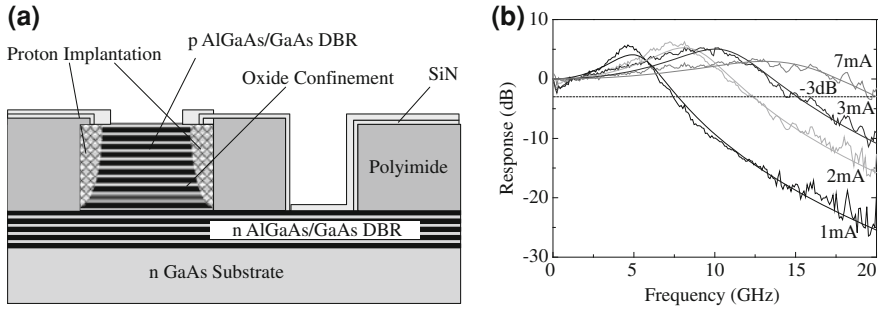
(a)

(b)

Fig. 7.11 a Cross-sectional schematic and **b** frequency responses of oxide-confined 6.9-µm-diameter 1.1-µm VCSELs [66] (© 2007 IEEE)
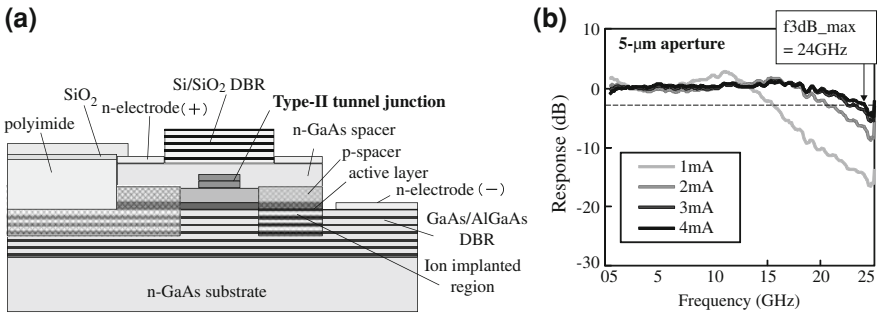
(a)

(b)

Fig. 7.12 a Structure and **b** frequency responses for 1.1-µm, BTJ VCSELs [67] (© 2008 OSA)

devices achieve a maximum bandwidth of 20 GHz at a bias of 7 mA, as shown in Fig. 7.11. Transmission at 30 Gb/s back-to-back and over 100-m multi-mode fiber have been done, and the power penalty is ∼2 dB.

The main limiting factor in their oxide-confined devices is self-heating effect, which causes the relaxation resonance frequency to saturate at high biases. To address this limitation, a low-resistance type-II BTJ is used so that the more resistive *p*-layer can be replaced with a less resistive *n*-spacer. The devices use top-emitting, double-intracavity structure shown in Fig. 7.12a.

The electrical and optical confinement is achieved by selectively etching the tunnel junction and regrowing the *n*-GaAs spacer layer. Oxygen ions are implanted around the tunnel junction to reduce the mesa capacitance. The pad capacitance is similarly reduced using polyimide. Dielectric Si/SiO$_2$ DBR is used for the top mirror.

Figure 7.12b plots the frequency responses for 5-µm-diameter devices. The maximum 3-dB frequency is 24 GHz at a bias current of 4 mA, which is the highest bandwidth reported for directly current-modulated VCSELs to date. A data rate of 40 Gb/s, which is also the highest data rate for VCSELs to date, is achieved using 6-µm devices at a bias current of 5 mA.

All these results were achieved at room temperature. To improve the high-temperature performance, they have also developed a new active region with strain-compensated $In_{0.3}Ga_{0.7}As/GaAs_{0.8}P_{0.2}$ QWs [68]. By increasing the conduction-band offset, electrons are better confined at the elevated temperature. A data rate of 25 Gb/s is achieved using oxide-confined structure.

7.4.4 Long-Wavelength VCSELs

Several technologies exist for LW-VCSELs, and they will be covered in more detail in Chaps. 11 and 12 of this book. The main application of high-speed LW-VCSELs is to use for optical networks, which currently require transmission up to 10 Gb/s over SMF. Here we summarize some current high-speed results for LW-VCSELs.

GaAs-Based Long-Wavelength VCSELs

GaAs-based LW-VCSELs are attractive due to the well-established technologies of short-wavelength VCSELs such as oxide apertures and bandgap-engineered, high-index-contrast DBRs. The main challenge is the choice of the gain media that can be pseudomorphically grown on GaAs substrates to reach longer emission wavelengths. Currently, GaAs-based LW-VCSELs are mainly operated below 1.3-μm wavelength, and there are three active region candidates [69]: highly strained InGaAs QWs, GaInNAs QWs, and InAs QDs.

The structure of GaAs-based LW-VCSELs is usually pretty similar to short-wavelength VCSELs except with a different gain media. Transmission at 10 Gb/s over 9-km SMF from 25°C to 85°C has been reported using highly strained InGaAs QWs emitting at 1.28 μm [13]. The indium content of the QWs is increased to 42% to push the gain peak to 1220 nm, and the cavity mode is detuned at 1275 nm, giving a large gain-cavity offset for better high-temperature stability [70]. An inverted surface relief is patterned on the top mirror for single-mode operation. However, the threshold current seems fairly high and reduces at higher temperature due to better cavity–gain alignment. The bandwidth is mostly limited by parasitics.
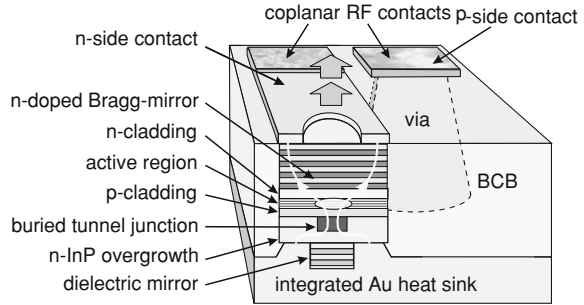
LW-VCSELs based on a GaInNAs active region emitting at 1.28 μm have also demonstrated 10-Gb/s transmission over 20-km SMF [11]. These devices show good reliability and have been placed into production [11, 71].

InP-Based Long-Wavelength VCSELs

For InP-based LW-VCSELs, the mature high-reliability InAlGaAs or InGaAsP active region can be used. The main issues are (a) the lack of DBR materials which provide high reflectivity and thermal conductivity, (b) the more extreme sensitivity to elevated temperatures, and (c) the realization of lateral mode confinement.

The first of these issues was addressed with an all-epitaxial approach using lattice-matched AlGaAsSb DBRs, which offer relatively high reflectivity, and an air-gap aperture formed by selectively etching tunnel junction. These have been explored

Fig. 7.13 Structure of
InP-based BTJ LW-VCSEL
[73] (© 2008 IEEE)

and demonstrated reasonable DC characteristics as well as 3.125-Gb/s operation up
to 60°C [72]. The poor electrical and thermal conductivity of the quaternary DBRs
was addressed by using *n*-type intracavity InP contact layers, but these also added to
the cavity length, which increased the cavity volume, and thus, reduced the frequency
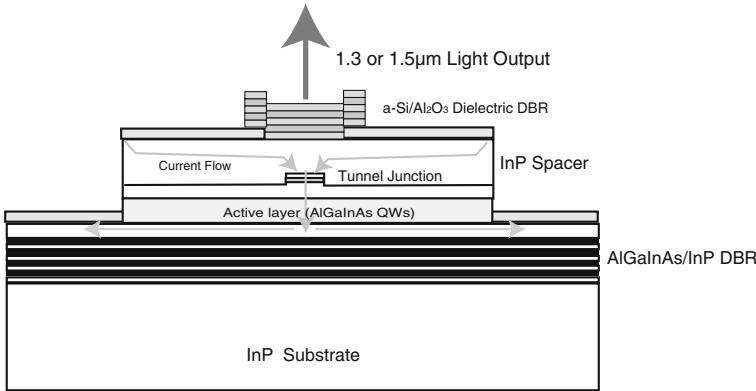response.

Another approach is to use BTJ, pioneered by Amann et al. at Walter Schottky
Institute. Some of the best high-speed performance for LW-VCSELs to date are
demonstrated based on this platform. Figure 7.13 shows the structure of their devices.
The lateral current and mode confinement is provided by the BTJ, which also enables
the regrown InP spacing layer to be *n*-type for lower loss and resistance. The back
mirror consists of several periods of CaF_2/ZnS dielectric DBR and a gold termination
layer, which also works as a heat sink. The device is passivated with BCB for high-
speed operation.

Based on this structure, bandwidth exceeding 10 GHz has been demonstrated for
both 1.3- and 1.55-µm wavelengths at room temperature [12, 51] and is limited by
parasitics and thermal effects. Transmission at 10 Gb/s for 22 km and 12.5 Gb/s for
3 km have also been reported at 1.3- and 1.55-µm wavelengths, respectively.

Corning also reported LW-VCSELs with 10-Gb/s transmission for both 1.3- and
1.55-µm wavelengths up to 85°C [10]. Their devices, shown in Fig. 7.14, are based
on similar BTJ technology with a dielectric top mirror. However, they use double-
intracavity contacts with top emission, which greatly simplifies the device structure
and can be mass manufactured more easily.

Wafer-Fused Long-Wavelength VCSELs

Both InP-based active region and GaAs-based DBRs are preferable for LW-VCSELs.
Therefore, wafer fusion, pioneered by Bowers et al. at University of California,
Santa Barbara, has been used to combine these two material systems. Transmission
at 10 Gb/s over 10-km standard SMF has been reported [44]. The structure consists
of undoped top and bottom AlGaAs/GaAs DBRs, wafer fused with InAlGaAs/InP
cavity grown on an InP substrate. A tunnel junction is used for lateral confinement.

Fig. 7.14 Cross-sectional schematic of BTJ LW-VCSELs with double-intracavity contacts [74] (©
2005 IEEE)

7.5 Loss-Modulated High-Speed VCSELs

Due to inherent damping limitations, it would be very challenging for directly current-
modulated VCSELs to reach bandwidth beyond 40 GHz, even after the parasitic and
thermal limitations have been removed. The highest modulation bandwidth to date is
still limited below 25 GHz [6]. Alternative approaches have to be pursued to extend
the bandwidth, e.g., optical injection locking and loss modulation. Optically injection
locked VCSELs have demonstrated an impressive modulation bandwidth of 66 GHz
based on a cascaded configuration [75]. However, a separated master laser is required.
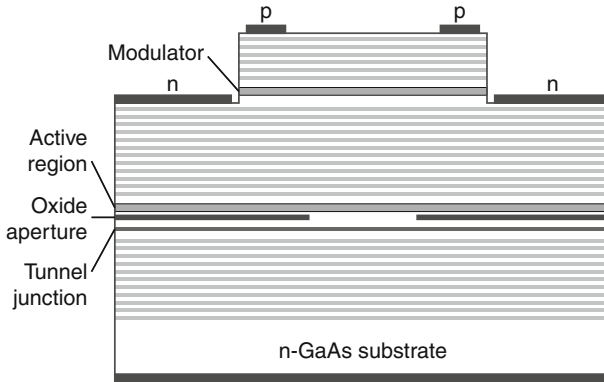Therefore, we only consider coupled-cavity loss-modulated VCSELs here.

7.5.1 Principle of Operation

All the devices that have been discussed so far are based on current modulation,
which is an indirect way to modulate the photon density. Alternatively, the photon
density can be modulated by varying the cavity loss, which has been theoretically
predicted to have higher modulation bandwidth [76].

In the rate equations discussed in Sect. 7.2, the losses are included through the
photon lifetime $\tau_p^{-1} = v_g(\alpha_i + \alpha_m)$, where α_i and α_m are the internal loss and mirror
loss, respectively. Here, we apply the small-signal analysis for loss modulation,
similar to (7.3a), by assuming

$$\frac{1}{\tau_p} = v_g(\alpha_0 + \alpha_1 e^{j\omega t}) = \frac{1}{\tau_{p0}}(1 + m e^{j\omega t}) \qquad (7.12)$$

where α_0 is the steady-state total loss, α_1 is the small-signal loss modulation ampli-
tude, $\tau_{p0} = (v_g\alpha_0)^{-1}$ is the steady-state photon lifetime, and $m = \alpha_1/\alpha_0$ is the loss

Fig. 7.15 Cross-sectional schematic of EAM-VCSEL [78]

modulation depth. Following the same procedure as we did for current modulation, the transfer function for loss-modulated intrinsic laser can be written as [77]

$$H_{\mathrm{L}}(\omega) = \frac{m}{\tau_{\mathrm{p}0}} \frac{\omega_{\mathrm{r}}^2 \tau_{\mathrm{p}} + j\omega}{(\omega_{\mathrm{r}}^2 - \omega^2 + j\omega\gamma)}. \tag{7.13}$$

The main difference between loss modulation and current modulation is the decay rate after the resonance: $1/\omega$ (20 dB/decade) for loss modulation and $1/\omega^2$ (40 dB/decade) for current modulation. In addition, the resonance peak is also stronger for loss modulation, which can be an issue for data transmission.

Two mechanisms have been used to achieve loss modulation in coupled-cavity VCSELs. One is to modulate the internal loss α_{i} using an electroabsorption modulator, and the other is to modulate the mirror loss α_{m} using an electrooptical modulator.

7.5.2 VCSELs with an Electroabsorption Modulator

Figure 7.15 shows the cross-sectional schematic of VCSEL with an intracavity electroabsorption modulator (EAM-VCSEL). It is basically a *p–n–p* configuration with a tunnel junction below the active region to reverse the polarity of the bottom contact. Reverse-biased MQW, placed at the standing-wave peak for maximal efficiency, is used as the modulator. A 17-GHz modulation bandwidth with a distinct 20 dB resonance peak has been reported [78]. The roll-off slope is ∼45 dB/decade with parasitics ($f_0 \sim$ 8 GHz), showing a slower decay rate compared with current-modulated devices.

Recently, the same group demonstrated optically decoupled loss modulation in a duo-cavity VCSELs by carefully detuning the resonances of the cavities [79]. The photon density in the active region remains unchanged under loss modulation, similar

to the case of using an external modulator with a continuous-wave laser. Relatively flat frequency responses up to 20 GHz have been shown.

7.5.3 VCSELs with an Electrooptical Modulator

Another possible way of achieving loss modulation is to integrate an electrooptical modulator in the VCSEL structure (EOM-VCSEL). The refractive index of the electrooptical modulator (MQW) can be tuned by an applied voltage. If properly designed, the cavity mode of the modulator cavity can be tuned in and out of the resonance of the VCSEL cavity, which effectively modulates the mirror reflectivity, i.e., the mirror loss α_m. Small-signal modulation bandwidth up to 35 GHz, limited by the photodiode, has been reported with EOM-VCSELs [80].

7.6 Conclusion

The chapter provides an overview of the current status for high-speed VCSELs. We discussed the basic theory for current modulation of VCSELs, various high-speed designs, and device performance. Novel structures and new material systems have been pursued to overcome many of the bandwidth limitations to achieve higher performance. For short-wavelength VCSELs, bandwidth up to 24 GHz and a data rate of 40 Gb/s have been successfully demonstrated. For LW-VCSELs, single-mode, 10-Gb/s transmission over a wide temperature range has also been reported by several groups. We also considered loss-modulated VCSELs which are still under development and have the potential to reach even higher bandwidth. As these technologies become more mature and the supporting components such as high-speed photodetectors are ready, VCSELs will be used as low-cost, power-efficient, high-speed light sources for most optical data communications.

References

1. D.A.B. Miller, Physical reasons for optical interconnection. Int. J. Optoelectronics **11**, 155 (1997)
2. D.M. Kuchta, P. Pepeljugoski, Y. Kwark, VCSEL modulation at 20Gb/s over 200m of multimode fiber using a 3.3v SiGe laser driver IC, in *Technical Digest LEOS Summer Topical Meeting*, Copper Mountain, CO (2001), p. 49

3. N. Suzuki, H. Hatakeyama, K. Fukatsu, T. Anan, K. Yashiki, M. Tsuji, 25-Gbps operation of 1.1-μm-range InGaAs VCSELs for high-speed optical interconnections, in *Proceedings of Optical Fiber Communication Conference*, *OFC 2006*, Anaheim, CA (2006)

4. K. Yashiki, N. Suzuki, K. Fukatsu, T. Anan, H. Hatakeyama, M. Tsuji, 1.1-μm-range tunnel junction VCSELs with 27-GHz relaxation oscillation frequency, in *Proceedings of Optical Fiber Communication Conference*, *OFC 2007*, Anaheim, CA (2007)

5. Y.-C. Chang, C.S Wang, L.A Coldren, High-efficiency, high-speed VCSELs with 35 Gbit/s error-free operation. Electron. Lett. **43**(19), 1022 (2007)

6. T. Anan, N. Suzuki, K. Yashiki, K. Fukatsu, H. Hatakeyama, T. Akagawa, K. Tokutome, M. Tsuji, High-speed InGaAs VCSELs for optical interconnects. in *Proceedings of International Symposium on VCSELs and Integrated Photonics*, paper E3, Tokyo, Japan (2007)

7. B.E. Lemoff, M.E. Ali, G. Panotopoulos, E. de Groot, G.M. Flower, G.H. Rankin, A.J. Schmit, K.D. Djordjev, M.R.T. Tan, A. Tandon, W. Gong, R.P. Tella, B. Law, D.W. Dolfi, Parallel-WDM for multi-Tb/s optical interconnects, in *Proceedings of IEEE Lasers and Electro-Optical Society Annual Meeting*, *LEOS 2005*, Sydney (2005), p. 359

8. C.L. Schow, F.E. Doany, O. Liboiron-Ladouceur, C. Baks, D.M. Kuchta, L. Schares, R. John, J.A. Kash, 160-Gb/s, 16-channel full-duplex, single-chip CMOS optical transceiver, in *Proceedings of Optical Fiber Communication Conference*, *OFC 2007*, Anaheim, CA (2007)

9. J. Cheng, C.-L. Shieh, X. Huang, G. Liu, M. Murty, C.C. Lin, D.X. Xu, Efficient CW lasing and high-speed modulation of 1.3-μm AlGaInAs VCSELs with good high temperature lasing performance. IEEE Photon. Technol. Lett. **17**(1), 7 (2005)

10. N. Nishiyama, C. Caneau, J.D. Downie, M. Sauer, C.-E. Zah, 10-Gbps 1.3 and 1.55-μm InP-based VCSELs: 85°C 10-km error-free transmission and room temperature 40-km transmission at 1.55-μm with EDC, in *Proceedings of Optical Fiber Communication Conference*, *OFC 2006*, Anaheim, CA (2006)

11. J. Jewell, L. Graham, M. Crom, K. Maranowski, J. Smith, T. Fanning, 1310 nm VCSELs in 1–10 Gb/s commercial applications, in *Vertical-Cavity Surface-Emitting Lasers X*, ed. by C. Lei, K.D. Choquette, Proceedings of SPIE, vol. 6132 (2007), p. 613204-1

12. W. Hofmann, N.H. Zhu, M. Ortsiefer, G. Böhm, Y. Liu, M.-C. Amann, High speed (> 11GHz) modulation of BCB-passivated 1.55μm InGaAlAs-InP VCSELs. Electron. Lett. **42**(17), 976 (2006)

13. E. Söderberg, J.S. Gustavsson, P. Modh, A. Larsson, Z. Zhang, J. Berggren, M. Hammar, High-temperature dynamics, high-speed modulation, and transmission experiments using 1.3-μm InGaAs single-mode VCSELs. J. Lightwave Technol. **25**(9), 2791 (2007)

14. R.S. Tucker, High-speed modulation of semiconductor lasers. J. Lightwave Technol. **3**(6), 1180 (1985)

15. L.A. Coldren, S.W. Corzine, *Diode Lasers and Photonic Integrated Circuits* (Wiley, New York, 1995)

16. D. Tauber, G. Wang, R.S. Geels, J.E. Bowers, L.A. Coldren, Large and small signal dynamics of vertical cavity surface emitting lasers. Appl. Phys. Lett. **62**(4), 325 (1993)

17. T.R. Chen, B. Zhao, L. Eng, Y.H. Zhuang, J. O'Brien, A. Yariv, Very high modulation efficiency of ultralow threshold current single quantum well InGaAs lasers. Electron. Lett. **29**(17), 1525 (1993)

18. R. Nagarajan, T. Fukushima, S.W. Corzine, J.E. Bowers, Effects of carrier transport on high-speed quantum well lasers. Appl. Phys. Lett. **59**(15), 1835 (1991)

19. Y. Liu, W.-C. Ng, B. Klein, K. Hess, Effects of the spatial nonuniformity of optical transverse modes on the modulation response of vertical-cavity surface-emitting lasers. IEEE J. Quantum Electron. **39**(1), 99 (2003)

20. J.W. Scott, R.S. Geels, S.W. Corzine, L.A. Coldren, Modeling temperature effects and spatial hole burning to optimize vertical-cavity surface-emitting laser performance. IEEE J. Quantum Electron. **29**(5), 1295 (1993)

21. S.F. Yu, W.N. Wong, P. Shum, E.H. Li, Theoretical analysis of modulation response and second-order harmonic distortion in vertical-cavity surface-emitting lasers. IEEE J. Quantum Electron. **32**(12), 2139 (1996)
22. M. Willatzen, T. Takahashi, Y. Arakawa, Nonlinear gain effects due to carrier heating and spectral hole burning in strained-quantum-well lasers. IEEE Photon. Technol. Lett. **4**(7), 682 (1992)
23. Y. Liu, W.-C. Ng, F. Oyafuso, B. Klein, K. Hess, Simulating the modulation response of VCSELs: the effects of diffusion capacitance and spatial hole-burning. IEE Proc. Optoelectron. **149**(4), 182 (2002)
24. J. Strologas, K. Hess, Diffusion capacitance and laser diodes. IEEE Trans. Electron Devices **51**(3), 506 (2004)
25. K.Y. Lau, A. Yariv, Ultra-high speed semiconductor lasers. IEEE J. Quantum Electron. **21**(2), 121 (1985)
26. Y. Arakawa, A. Yariv, Quantum well lasers—gain, spectra, dynamics. IEEE J. Quantum Electron. **22**(9), 1887 (1986)
27. J.D. Ralston, S. Weisser, I. Esquivias, E.C. Larkins, J. Rosenzweig, P.J. Tasker, J. Fleissner, Control of differential gain, nonlinear gain, and damping factor for high-speed application of GaAs-based MQW lasers. IEEE J. Quantum Electron. **29**(6), 1648 (1993)
28. A. Schönfelder, S. Weisser, I. Esquivias, J.D. Ralston, J. Rosenzweig, Theoretical investigation of gain enhancements in strained $In_{0.35}Ga_{0.65}As/GaAs$ MQW lasers via p-doping. IEEE Photon. Technol. Lett. **6**(4), 475 (1994)
29. B. Zhao, T.R. Chen, A. Yariv, The extra differential gain enhancement in multiple-quantum-well lasers. IEEE Photon. Technol. Lett. **4**(2), 124 (1992)
30. K.L. Lear, R.P. Schneider Jr., K.D. Choquette, S.P. Kilcoyne, Index guiding dependent effects in implant and oxide confined vertical-cavity lasers. IEEE Photon. Technol. Lett. **8**(6), 740 (1996)
31. Y. Satuby, M. Orenstein, Limits of the modulation response of a single-mode proton implanted VCSEL. IEEE Photon. Technol. Lett. **10**(6), 760 (1998)
32. A.N. AL-Omari, K.L. Lear, Polyimide-planarized vertical-cavity surface-emitting lasers with 17.0-GHz bandwidth. IEEE Photon. Technol. Lett. **16**(4), 969 (2004)
33. K.L. Lear, A. Mar, K.D. Choquette, S.P. Kilcoyne, R.P. Schneider Jr., K.M. Geib, High-frequency modulation of oxide-confined vertical cavity surface emitting lasers. Electron. Lett. **32**(5), 457 (1996)
34. P. Westbergh, J.S. Gustavsson, Å. Haglund, H. Sunnerud, A. Larsson, Large aperture 850 nm VCSELs operating at bit rates up to 25 Gbit/s. Electron. Lett. **4**(15), 907 (2008)
35. B.J. Thibeault, K. Bertilsson, E.R. Hegblom, E. Strzelecka, P.D. Floyd, R. Naone, L.A. Coldren, High-speed characteristics of low-optical loss oxide-apertured vertical-cavity lasers. IEEE Photon. Technol. Lett. **9**(1), 11 (1997)
36. Y.-C. Chang, C.S. Wang, L.A. Johansson, L.A. Coldren, High-efficiency, high-speed VCSELs with deep oxidation layers. Electron. Lett. **42**(22), 1281 (2006)
37. R.H. Johnson, D.M. Kuchta, 30 Gb/s directly modulated 850 nm datacom VCSELs, in *Conference on Lasers and Electro-Optics*, CLEO 2008, San Jose, CA (2008)
38. E.R. Hegblom, D.I. Babic, B.J. Thibeault, L.A. Coldren, Scattering losses from dielectric apertures in vertical-cavity lasers. IEEE J. Select. Topics Quantum Electron. **3**(2), 379 (1997)
39. L.A. Coldren, E.R. Hegblom, Fundamental issues in VCSEL design. Chap. 2 in *Vertical-Cavity Surface-Emitting Lasers*, ed. by C. Wilmsen, H. Temkin, L.A. Coldren (Cambridge University Press, Cambridge, 1999), pp. 32–67
40. Y.H. Chang, H.C. Kuo, F.-I. Lai, K.F. Tzeng, H.C. Yu, C.P. Sung, H.P. Yang, S.C. Wang, High speed (>13 GHz) modulation of 850 nm vertical cavity surface emitting lasers (VCSELs) with tapered oxide confined layer. IEE Proc. Optoelectron. **152**(3), 170 (2005)
41. Å. Haglund, J.S. Gustavsson, P. Modh, A. Larsson, Dynamic mode stability analysis of surface relief VCSELs under strong RF modulation. IEEE Photon. Technol. Lett. **17**(8), 1602 (2005)

42. C.C. Chen, S.J. Liaw, Y.J. Yang, Stable single-mode operation of an 850-nm VCSEL with a higher order mode absorber formed by shallow Zn diffusion. IEEE Photon. Technol. Lett. **13**(4), 266 (2001)

43. J.-W. Shi, C.-C. Chen, Y.-S. Wu, S.-H. Guol, C. Kuo, Y.-J. Yang, High-power and high-speed Zn-diffusion single fundamental-mode vertical-cavity surface-emitting lasers at 850-nm wavelength. IEEE Photon. Technol. Lett. **20**(13), 1121 (2008)

44. A. Syrbu, A. Mereuta, V. Iakovlev, A. Caliman, P. Royo, E. Kapon, 10 Gbps VCSELs with high single mode output in 1310 nm and 1550 nm wavelength bands, in *Proceedings of Optical Fiber Communication Conference*, *OFC 2008*, San Diego, CA (2008)

45. K.L. Lear, A.N. Al-Omari, Progress and issues for high-speed vertical cavity surface emitting lasers, in *Vertical-Cavity Surface-Emitting Lasers XI*, ed. by K.D. Choquette, J.K. Guenter, Proceedings of SPIE, vol. 6484 (2007), p. 64840J-1

46. Y.-C. Chang, L.A. Coldren, Efficient, high-data-rate, tapered oxide-aperture vertical-cavity surface-emitting lasers. IEEE J. Select. Topics Quantum Electron. **15**(3), 704 (2009)

47. C.-K. Lin, A. Tandon, K. Djordjev, S.W. Corzine, M.R.T. Tan, High-speed 985 nm bottom-emitting VCSEL arrays for chip-to-chip parallel optical interconnects. IEEE J. Select. Topics Quantum Electron. **13**(5), 1332 (2007)

48. M.G. Peters, B.J. Thibeault, D.B. Young, J.W. Scott, F.H. Peters, A.C. Gossard, L.A. Coldren, Band-gap engineered digital alloy interfaces for lower resistance vertical-cavity surface-emitting lasers. Appl. Phys. Lett. **63**(25), 3411 (1993)

49. K.L. Lear, R.P Schneider Jr., Uniparabolic mirror grading for vertical cavity surface emitting lasers. Appl. Phys. Lett. **68**(5), 605 (1996)

50. K.L. Lear, V.M. Hietala, H.Q. Hou, J. Banas, B.E. Hammons, J. Zolper, S.P. Kilcoyne, Small and large signal modulation of 850 nm oxide-confined vertical-cavity surface-emitting lasers, in *Conference on Lasers and Electro-Optics*, *CLEO'97*, Baltimore, MD (1997)

51. M. Ortsiefer, W. Hofmann, E. Rönneberg, A. Boletti, A. Gatto, P. Boffi, J. Rosskopf, R. Shau, C. Neumeyr, G. Böhm, M. Martinelli, M.-C. Amann, High speed 1.3μm VCSELs for 12.5 Gbit/s optical interconnects. Electron. Lett. **44**(16), 974 (2008)

52. D.L. Mathine, H. Nejad, D.R. Allee, R. Droopad, G.N. Maracas, Reduction of the thermal impedance of vertical-cavtiy surface-emitting lasers after integration with copper substrates. Appl. Phys. Lett. **69**(4), 463 (1996)

53. T. Wipiejewski, D.B. Young, M.G. Perers, B.J. Thibeault, L.A. Coldren, Improved performance of vertical-cavity surface-emitting laser diodes with Au-plated heat spreading layer. Electron. Lett. **31**(4), 279 (1995)

54. A.N. AL-Omari, G.P Carey, S. Hallstein, J.P. Watson, G. Dang, K.L. Lear, Low thermal resistance high-speed top-emitting 980-nm VCSELs. IEEE Photon. Technol. Lett. **18**(11), 1225 (2006)

55. Y.-C. Chang, L.A. Coldren, Optimization of VCSEL structure for high-speed operation, in *Proceedings of IEEE International Semiconductor Laser Conference*, *ISLC 2008*, Sorrento, Italy (2008), p. 159

56. D.B. Young, J.W. Scott, F.H. Peters, M.G. Peters, M.L. Majewski, B.J. Thibeault, S.W. Corzine, L.A. Coldren, Enhanced performance of offset-gain high-barrier vertical-cavity surface-emitting lasers. IEEE J. Quantum Electron. **29**(6), 2013 (1993)

57. J. Ko, E.R. Hegblom, Y. Akulova, B.J. Thibeault, L.A. Coldren, Low-threshold 840-nm laterally oxidized vertical-cavity lasers using AlInGaAs-AlGaAs strained active layers. IEEE Photon. Technol. Lett. **9**(7), 863 (1997)

58. H.C. Kuo, Y.S. Chang, F.Y. Lai, T.H. Hsueh, L.H. Laih, S.C. Wang, High-speed modulation of 850 nm InGaAsP/InGaP strain-compensated VCSELs. Electron. Lett. **39**(14), 1051 (2003)

59. T. Aggerstam, R.M.V. Würtemberg, C. Runnström, E. Choumas, Large aperture 850 nm oxide-confined VCSELs for 10 Gb/s data communication, in *Vertical-Cavity Surface-Emitting Lasers VI*, ed. by C. Lei, S.P. Kilcoyne, Proceedings of SPIE, vol. 4649 (2002), p. 19

60. S.L. Yellen, A.H. Shepard, R.J. Dalby, J.A. Baumann, H.B. Serreze, T.S. Guido, R. Soltz, K.J. Bystrom, C.M. Harding, R.G. Waters, Reliability of GaAs-based semiconductor diode lasers: 0.6–1.1μm. IEEE J. Quantum Electron. **29**(6), 2058 (1993)

61. P. Westbergh, J.S. Gustavsson, Å. Haglund, A. Larsson, H. Hopfer, G. Fiol, D. Bimberg, A. Joel, 32 Gbit/s multimode fibre transmission using a high speed, low current density 850 nm VCSEL. Electron. Lett. **45**(7), 366 (2009)

62. S.A. Blokhin, J.A. Lott, A. Mutig, G. Fiol, N.N. Ledentsov, M.V. Maximov, A.M. Nadtochiy, V.A. Shchukin, D. Bimberg, 40 Gbit/s oxide-confined 850 nm VCSELs. Electron. Lett. **45**(10), 501 (2009)

63. F. Hopfer, A. Mutig, G. Fiol, M. Kuntz, S.S. Mikhrin, I.L. Krestnikov, D.A. Livshits, A.R. Kovsh, C. Bornholdt, V. Shchukin, N.N. Ledentsov, V. Gaysler, N.D. Zakharov, P. Werner, D. Bimberg, 20 Gb/s direct modulation of 980 nm VCSELs based on submonolayer deposition of quantum dots, in *Workshop on Optical Components for Broadband Communication*, ed. by P.-Y. Fonjallaz, T.P. Pearsall, Proceedings of SPIE, vol. 6350 (2006), p. 635003-1

64. A. Mutig, G. Fiol, P. Moser, F. Hopfer, M. Kuntz, V. Shchukin, N. Ledentsov, D. Bimberg, S. Mikhrin, I. Krestnikov, D. Livshits, A. Kovsh, 120 °C 20 Gbit/s operation of 980 nm single mode VCSEL, in *Proceedings of IEEE International Semiconductor Laser Conference*, *ISLC 2008*, Sorrento, Italy (2008), p. 9

65. N. Suzuki, H. Hatakeyama, K. Tokutome, M. Yamada, T. Anan, M. Tsuji, 1.1μm range InGaAs VCSELs for high-speed optical interconnections, in *Proceedings of IEEE Lasers and Electro-Optical Society Annual Meeting*, *LEOS 2005*, Sydney (2005), p. 394

66. K. Fukatsu, K. Shiba, Y. Suzuki, N. Suzuki, H. Hatakeyama, T. Anan, K. Yashiki, M. Tsuji, 30-Gbps transmission over 100 m-MMFs (GI32) using 1.1 μm-range VCSELs and receivers, in *Proceedings of International Conference on Indium Phosphide and Related Materials*, Matsue, Japan (2007), p. 434

67. T. Anan, N. Suzuki, K. Yashiki, K. Fukatsu, H. Hatakeyama, T. Akagawa, K. Tokutome, M. Tsuji, *High-speed* 1.1-μm-range InGaAs VCSELs, in *Proceedings of Optical Fiber Communication Conference*, *OFC 2008*, San Diego, CA (2008)

68. H. Hatakeyama, T. Anan, T. Akagawa, K. Fukatsu, N. Suzuki, K. Tokutome, M. Tsuji, Highly reliable high speed 1.1μm-InGaAs/GaAsP-VCSELs, in *Vertical-Cavity Surface-Emitting Lasers XIII*, ed. by K.D. Choquette, C. Lei, Proceedings of SPIE, vol. 7229 (2009), p. 722902-1

69. P. Gilet, E. Pougeoise, L. Grenouillet, P. Grosse, N. Olivier, S. Poncet, A. Chelnokov, J.M. Gérard, R. Stevens, R. Hamelin, M. Hammar, J. Berggren, P. Sundgren, 1.3μm VCSELs: InGaAs/GaAs, GaInNAs/GaAs multiple quantum wells and InAs/GaAs quantum dots—three candidates as active material, in *Vertical-Cavity Surface-Emitting Lasers XI*, ed. by K.D. Choquette, J.K. Guenter, Proceedings of SPIE, vol. 6484 (2007), p. 64840F-1

70. S. Mogg, N. Chitica, U. Christiansson, R. Schatz, P. Sundgren, C. Asplund, M. Hammar, Temperature sensitivity of the threshold current of long-wavelength InGaAs-GaAs VCSELs with large gain-cavity detuning. IEEE J. Quantum Electron. **40**(5), 453 (2004)

71. J. Jewell, L. Graham, M. Crom, K. Maranowski, J. Smith, T. Fanning, M. Schnoes, Commercial GaInNAs VCSELs grown by MBE. Phys. Status Solidi C **5**(9), 2951 (2008)

72. D. Feezell, L.A. Johansson, D.A. Buell, L.A. Coldren, Efficient modulation of InP-based 1.3-μmVCSELs with AsSb-based DBRs. IEEE Photon. Technol. Lett. **17**(11), 2253 (2005)

73. W. Hofmann, M. Ortsiefer, E. Rönneberg, C. Neumeyr, G. Böhm, M.-C. Amann, 1.3μm InGaAlAs/InP VCSEL for 10G Ethernet, in *Proceedings of IEEE International Semiconductor Laser Conference*, *ISLC 2008*, paper MB3, Sorrento, Italy (2008)

74. N. Nishiyama, C. Caneau, B. Hall, G. Guryanov, M.H. Hu, X.S. Liu, M.-J. Li, R. Bhat, C.E. Zah, Long-wavelength vertical-cavity surface-emitting lasers on InP with lattice matched AlGaInAs-InP DBR grown by MOCVD. IEEE J. Select. Topics Quantum Electron. **11**(5), 990 (2005)

75. X. Zhao, D. Parekh, E.K. Lau, H.-K. Sung, M.C. Wu, W. Hofmann, M.C. Amann, C.J. Chang-Hasnain, Novel cascaded injection-locked 1.55-μmVCSELs with 66 GHz modulation bandwidth. Opt. Express **15**(22), 14810 (2007)

76. E.A. Avrutin, V.B. Gorfinkel, S. Luryi, K.A. Shore, Control of surface-emitting laser diodes by modulating the distributed Bragg mirror reflectivity: small-signal analysis. Appl. Phys. Lett. **63**(18), 2460 (1993)
77. J. van Eisden, M. Yakimov, V. Tokranov, M. Varanasi, O. Rumyantsev, E.M. Mohammed, I.A. Young, S.R. Oktyabrsky, High frequency resonance-free loss modulation in a duo-cavity VCSEL, in *Vertical-Cavity Surface-Emitting Lasers XII*, ed. by C. Lei, J.K. Guenter, Proceedings of SPIE, vol. 6908 (2008), p. 69080M-1
78. J. van Eisden, M. Yakimov, V. Tokranov, M. Varanasi, E.M. Mohammed, I.A. Young, S. Oktyabrsky, Modulation properties of VCSEL with intracavity modulator, in *Vertical-Cavity Surface-Emitting Lasers XI*, ed. by K.D. Choquette, J.K. Guenter, Proceedings of SPIE, vol. 6484 (2007), p. 64840A-1
79. J. van Eisden, M. Yakimov, V. Tokranov, M. Varanasi, E.M. Mohammed, I.A. Young, S.R. Oktyabrsky, Optically decoupled loss modulation in a duo-cavity VCSEL. IEEE Photon. Technol. Lett. **20**(1), 42 (2008)
80. A. Paraskevopoulos, H.J. Hensel, W.D. Molzow, H. Klein, N. Grote, N.N. Ledentsov, V.A. Shchukin, C. Möller, A.R. Kovsh, D.A. Livshits, I.L. Krestnikov, S.S. Mikhrin, P. Matthijsse, G. Kuyt, Ultra-high-bandwidth (>35 GHz) electrooptically-modulated VCSEL, in *Proceedings of Optical Fiber Communication Conference*, *OFC 2006* Anaheim, CA (2006)